

CrossMark  
click for updates

Cite this: DOI: 10.1039/c4ta05237d

# Optical properties of organometal halide perovskite thin films and general device structure design rules for perovskite single and tandem solar cells†

Chang-Wen Chen, Sheng-Yi Hsiao, Chien-Yu Chen, Hao-Wei Kang,  
Zheng-Yu Huang and Hao-Wu Lin\*Received 2nd October 2014  
Accepted 28th October 2014

DOI: 10.1039/c4ta05237d

www.rsc.org/MaterialsA

The optical constants of a  $\text{CH}_3\text{NH}_3\text{PbI}_{3-x}\text{Cl}_x$  perovskite thin film were acquired for the first time. With this optical constant information, detailed optical modelling and optimization were performed and the calculations suggest that power conversion efficiencies of up to 20% and 29% are feasible in planar-type single and tandem cells.

Organometal halide perovskites ( $\text{ABX}_3$ , A:  $\text{CH}_3\text{NH}_3$ ,  $\text{HNCHNH}_3$ , B: Pb, Sn, X: Cl, Br, and I) have recently attracted considerable attention as promising materials for solar energy conversion.<sup>1–10</sup> Planar-type perovskite solar cells are particularly interesting due to their simple structures, low-temperature, low-power-consumption, and possibility for roll-to-roll manufacturing on flexible substrates.<sup>11–21</sup> High absorption coefficients have been found in these perovskite materials, which are prerequisites for efficient solar cells.<sup>7,8,16,17</sup> Surprisingly, however, detailed optical constant information, including the wavelength-dependent refractive index ( $n$ ), extinction coefficient ( $k$ ) and dielectric constant ( $\epsilon$ ), has not yet been reported. This could be due to the high roughness of perovskite thin films, complicated perovskite-metal oxide composites and complex multi-underlayer structures, which make determining the optical properties of organometal halide perovskites difficult. We recently developed a novel sequential layer-by-layer deposition method for fabricating organometal halide perovskite thin films.<sup>22</sup> The resulting films exhibit a pin-hole-free homogenous morphology with a low root mean squared roughness ( $R_{\text{rms}}$ ) of  $\sim 23$  nm. Furthermore, the films can be fabricated on poly(3,4-ethylenedioxythiophene)-poly(styrenesulfonate) (PEDOT : PSS) and

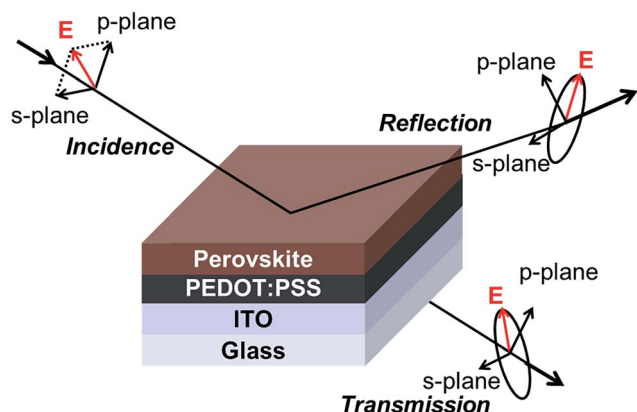
indium tin oxide (ITO) electrodes, which also possess low surface roughnesses. Since in ellipsometric measurement, a surface roughness of less than 55 nm or  $\sim 30\%$  of the probe wavelength is required,<sup>23,24</sup> these relatively flat layer-by-layer structures provide a great opportunity for investigating the optical properties of perovskite thin films.

In this study, the complex refractive indices (and dielectric functions) of organometal halide perovskites ( $\text{CH}_3\text{NH}_3\text{PbI}_{3-x}\text{Cl}_x$ ) in the wavelength range of 300 to 1100 nm were determined for the first time. These data are extremely important for designing the optical structures of perovskite solar cells. Through simulations using the transfer matrix method, design rules for the device, including the selection of electron- and hole-transporting layers (ETLs/HTLs), optimisation of the layer thickness of individual films and carrier balance of tandem cells, were obtained. The results provide a general overview of favourable optical designs for perovskite photovoltaics, which is believed will accelerate the progress in perovskite solar cell development towards power conversion efficiencies (PCE) exceeding 20%.

Variable-angle spectroscopic ellipsometry (VASE) was used to study the optical constants of perovskite films. Scheme 1 shows the configuration of the sample used in the measurement. The perovskite films, PEDOT : PSS and ITO underlayers, were prepared using the same conditions employed for high-efficiency device fabrication.<sup>22</sup> Because of the complicated interference of the multi-layer structure and the coupling of parameters in the optical constants and layer thickness, it is difficult to determine all of the desired parameters, including wavelength-dependent optical constants and layer thicknesses, of all the layers in a single VASE measurement. Hence, we used a “divide and conquer” approach to accurately obtain the optical constants of the samples layer-by-layer. We first measured the ellipsometric data of glass/ITO. The optical constants of ITO can

Department of Materials Science and Engineering, National Tsing Hua University, No. 101, Section 2, Kuang-Fu Road, Hsinchu, Taiwan 30013. E-mail: hwl@mx.nthu.edu.tw

† Electronic supplementary information (ESI) available: Experimental methods; optical constants of ITO, PEDOT : PSS,  $\text{CH}_3\text{NH}_3\text{PbI}_{3-x}\text{Cl}_x$ , PTB7, PBDTTT-C-T, GaAs, CdTe, CIGS,  $\text{PC}_{60}\text{BM}$ , Spiro-OMeTAD and ZnO thin films; cross-section SEM image and dielectric constant of  $\text{CH}_3\text{NH}_3\text{PbI}_{3-x}\text{Cl}_x$  thin films; the simulated  $J_{\text{sc}}$  vs. perovskite layer thickness of the normal-type device with and without Bphen and Ca thin films; the E.Q.E. and reflectance spectra of the normal-type device with  $\text{MoO}_3$  and  $\text{WO}_3$  as HTLs and the inverted-type device with ZnO as the ETL; The contour plot of mismatched  $J_{\text{sc}}$  values; the achievable  $J_{\text{sc}}$  of the perovskite/CIGS tandem cell with respect to the AZO and perovskite layer thicknesses; the reflectance spectrum of the optimised perovskite-CIGS tandem device. See DOI: 10.1039/c4ta05237d

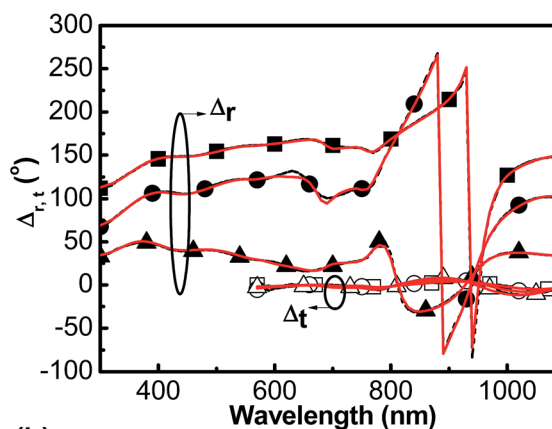
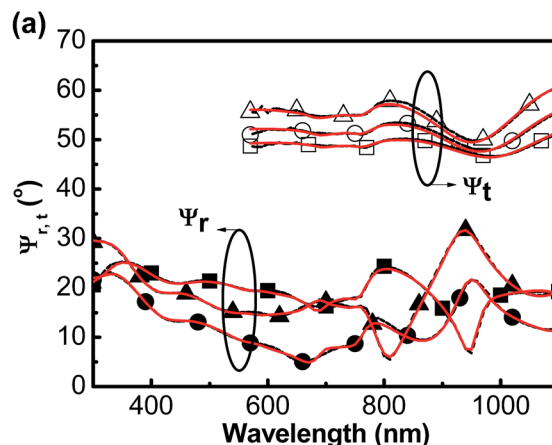


Scheme 1 Schematic illustration of the perovskite sample measured using VASE in reflection and transmission modes.

be well fitted using a Kramers–Kronig consistent model, which consists of a combination of a Gaussian oscillator in the ultra-violet wavelength range and a Drude model to account for free carrier absorption in the highly conductive ITO.<sup>25–27</sup> The optical constants of ITO were obtained and are shown in Fig. S1.† We then measured the VASE data of the glass/ITO/PEDOT : PSS sample. The thickness and optical properties of ITO were treated as known parameters during the analysis of the glass/ITO/PEDOT : PSS sample. Although some PEDOT : PSS films were found to be optically anisotropic with different optical constants normal to the surface compared to in-plane values, in our case, an isotropic model could well fit the ellipsometric results.<sup>28</sup> This could be due to the thin thickness ( $\sim 40$  nm) of PEDOT : PSS that we used because optical anisotropy is indistinguishable in such a thin layer. The extracted optical constants for the PEDOT : PSS film are shown in Fig. S2,† and these constants were subsequently treated as known parameters in the glass/ITO/PEDOT : PSS/perovskite sample. Finally, a perovskite film was fabricated on a glass/ITO/PEDOT : PSS substrate and measured using VASE.

To examine the optical constants in both the transparent and absorption regions of the complex multi-layer samples with some surface roughness, more ellipsometric data other than those from typical reflection ellipsometry measurements are required to reduce correlation and to acquire accurate results due to the high degree of correlation between model parameters.<sup>29,30</sup> Approaches such as multi-sample analysis, combining results from reflection ellipsometry and the absorption spectrum of a sample, or combining data from both reflection and transmission ellipsometry are generally used.<sup>31,32</sup> In this study, the optical constants of the perovskite thin film were determined using a combination of reflection and transmission ellipsometric measurements of a single sample, which eliminates the risk of sample-to-sample variation that could occur in a multi-sample analysis.<sup>33–35</sup>

Fig. 1(a) shows the ellipsometric data measured for the glass/ITO/PEDOT : PSS/perovskite sample. Due to the very high absorption of the perovskite layer in the wavelength range of 300 to 550 nm, no transmission ellipsometric data could be



(b)

EMA / 95 % void	42 nm
EMA / 7.32 % void	72 nm
Perovskite	360 nm
PEDOT:PSS	40 nm
ITO	141 nm
Glass	

Fig. 1 (a) Experimental (dashed lines) and the fitted (solid lines) ellipsometric parameters,  $\Psi_{r,t}$  and  $\Delta_{r,t}$  of the glass/ITO/PEDOT : PSS/perovskite sample. The measured parameters and fittings are in transmission mode at incident angles of  $40^\circ$  ( $\square$ ),  $50^\circ$  ( $\circ$ ), and  $60^\circ$  ( $\triangle$ ) and in reflection mode at incident angles of  $55^\circ$  ( $\blacksquare$ ),  $65^\circ$  ( $\bullet$ ), and  $75^\circ$  ( $\blacktriangle$ ). (b) The model configuration and the extracted layer parameters of the best fitting result.

obtained at these wavelengths. Initially, the thickness of the perovskite thin film was determined by assuming that  $n$  obeyed the Cauchy equation and that  $k = 0$  in the transparent region (900–1100 nm). With the obtained perovskite layer thickness, the values of  $n$  and  $k$  were independently varied wavelength-by-wavelength across the entire spectral range to fit the ellipsometric data ( $\Psi$  and  $\Delta$ ). The extracted wavelength-by-wavelength

optical constants were then used as the initial values to construct a Kramers–Kronig consistent oscillator model. Five Gaussian oscillators were used in the model to describe the absorption of the perovskite film. The oscillator model was then used to directly fit the measured  $\Psi$  and  $\Delta$  data to ensure Kramers–Kronig consistency. Because slight surface roughness had already been observed in the perovskite films using scanning electron microscopy (SEM), as shown in Fig. S3,<sup>†</sup> effective medium approximation (EMA) layers consisting of perovskite and a certain percentage of voids (air) were used to account for this morphology.<sup>36–38</sup> Fig. 1(b) shows the model configuration and the extracted layer thicknesses for the best fitting results. The fittings are shown in Fig. 1(a). Good agreement was found between the measured and fitted data. The extracted layer thicknesses and EMA layers representing surface roughness were all also in good agreement with the cross-sectional SEM image shown in Fig. S3. The resulting optical constants and dielectric constants of the  $\text{CH}_3\text{NH}_3\text{PbI}_{3-x}\text{Cl}_x$  thin film are shown in Fig. 2 and S4.<sup>†</sup> The film shows extinction coefficient peaks at 355 nm, 460 nm, 630 nm and 730 nm with  $k$  values of 1.29, 0.75, 0.30 and 0.26, respectively, and the refractive index is approximately 2.4–2.6 in the visible to near-infrared wavelength range. Comparisons of the perovskite extinction coefficients with common organic and inorganic photovoltaic materials are shown in Fig. S5.<sup>†</sup> The  $k$  values of the perovskite are slightly higher than those of inorganic materials such as CIGS, GaAs and CdTe in the wavelength range of 450 nm to 750 nm.<sup>39–41</sup> Compared with state-of-the-art organic photovoltaic materials such as poly{[4,8-bis[(2-ethylhexyl)oxy]benzo[1,2-*b*:4,5-*b'*]dithiophene-2,6-diyl}{3-fluoro-2-[(2-ethylhexyl)carbonyl]thieno[3,4-*b*]thiophenediyl} (PTB7) and poly{[4,8-bis-(2-ethyl-hexyl-thiophene-5-yl)-benzo[1,2-*b*:4,5-*b'*]dithiophene-2,6-diyl}-*alt*-[2-(2'-ethyl-hexanoyl)-thieno[3,4-*b*]thiophen-4,6-diyl]} (PBDTTT-C-T), the perovskite film shows a higher  $k$  value in the ultra-violet and blue-to-green wavelength range but a lower  $k$  value in the red wavelength range. Interestingly, as shown in Fig. S6,<sup>†</sup> the perovskite film also exhibits a lower refractive index than that of CIGS, GaAs and CdTe, which will result in lower reflection at the perovskite/electrode interface. This result indicates that anti-reflection coatings could be considerably easier to design or even not necessarily required for perovskite solar cells compared to other inorganic photovoltaic technologies.

We developed a panchromatic optical simulation program based on the transfer matrix method. This program has been utilised to design optical structures for organic microcavities and tandem solar cells.<sup>42–45</sup> Because the device structure of planar-type perovskite solar cells is similar to that of organic thin-film solar cells, the simulation should be well adopted in the design of perovskite solar cells. In the program, the short circuit current density ( $J_{\text{sc}}$ ) was calculated by integrating the product of standard AM 1.5G, 1 sun photon flux density and external quantum efficiency (E.Q.E.) over the entire wavelength range.<sup>46</sup> No carrier recombination loss is assumed after the conversion of photons into free carriers. To accurately calculate the spectral response and integrated  $J_{\text{sc}}$  of the device, wavelength-dependent optical constants of each layer in the device structure are needed. With the exception of  $n$ , the  $k$  values of the

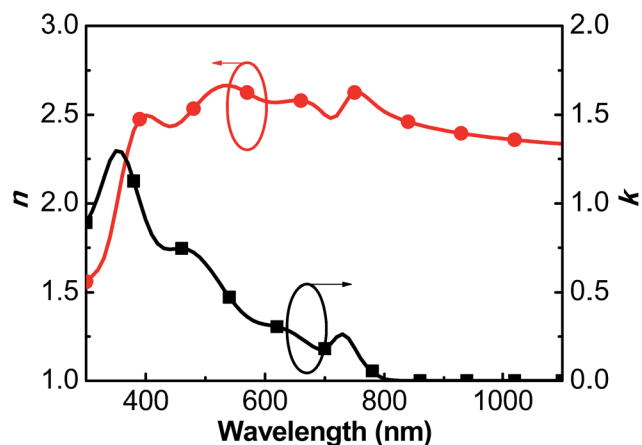


Fig. 2 Refractive index ( $n$ ) and extinction coefficient ( $k$ ) spectra of  $\text{CH}_3\text{NH}_3\text{PbI}_{3-x}\text{Cl}_x$  thin films.

perovskite thin film that have been obtained with the above-mentioned procedure, the optical constants of HTLs and ETLs, were all carefully measured with VASE before inputting them as parameters in the simulation program. The optical constants of these layers are summarised in Fig. S7.<sup>†</sup>

Schematics of the device structures for the simulation are shown in Fig. 3. Analogous to the device structures used in organic thin-film solar cells, both normal and inverted structures can be adopted with perovskite active materials. Typical HTLs used in the normal structure are PEDOT : PSS and *p*-type metal oxides such as  $\text{MoO}_3$ ,  $\text{WO}_3$  and  $\text{V}_2\text{O}_5$ , whereas fullerenes (*e.g.*  $\text{C}_{60}$ , [6,6]-phenyl-C61-butyric acid methyl ester ( $\text{PC}_{60}\text{BM}$ )) are usually utilised as ETLs.<sup>47–50</sup> In the inverted structure, *n*-type metal-oxides, such as  $\text{ZnO}$  and  $\text{TiO}_2$ , are typically used as ETLs, and organic HTLs such as [6,6]-phenyl-C61-butyric acid methyl ester (Spiro-OMeTAD) can be used as HTLs.<sup>18</sup> Recently, Colella *et al.* demonstrated that the chlorine atoms of  $\text{CH}_3\text{NH}_3\text{PbI}_{3-x}\text{Cl}_x$  are preferentially located in close proximity to the perovskite/ $\text{TiO}_2$  interface, which will affect the transport properties and recombination

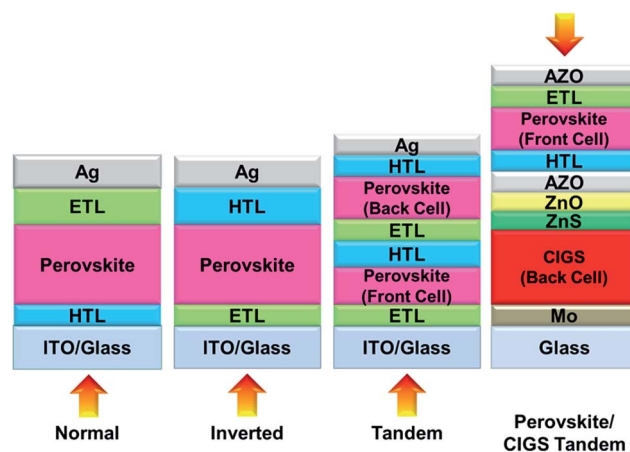
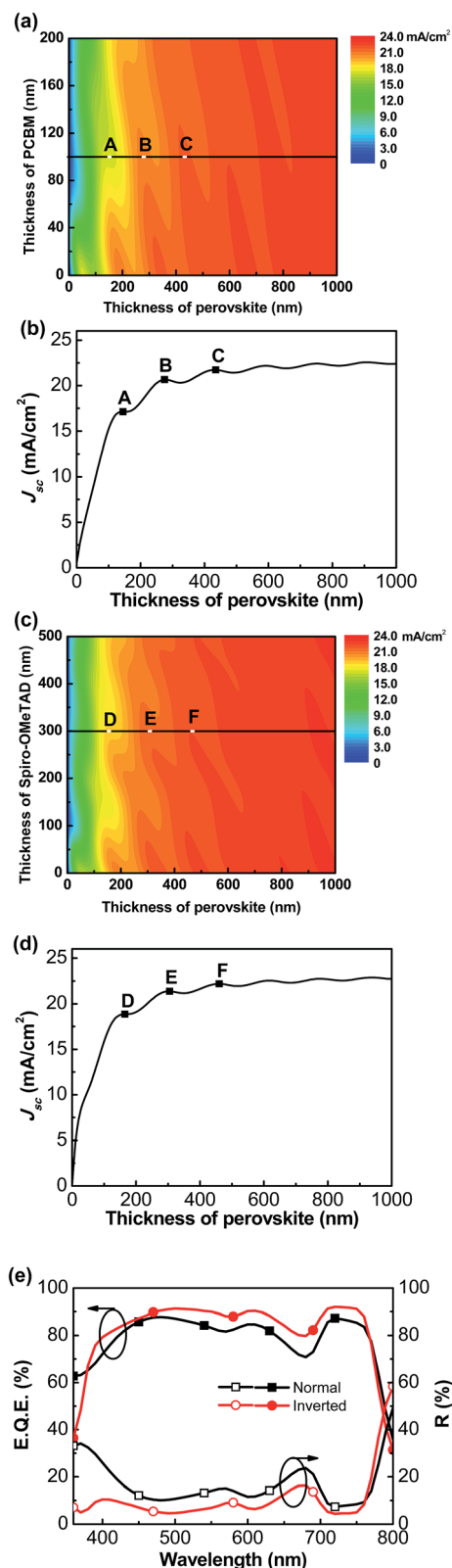


Fig. 3 The schematics of device structures for simulations. The arrows indicate the incident light direction. ITO: indium tin oxide. HTL: hole-transporting layer. ETL: electron-transporting layer.



**Fig. 4** (a) The contour plot of simulated  $J_{sc}$  vs. perovskite and PC<sub>60</sub>BM thicknesses of the normal-type device. Device structure: ITO (140 nm)/PEDOT : PSS (40 nm)/perovskite (0–1000 nm)/PC<sub>60</sub>BM (0–200 nm)/Ag (120 nm). (b) The simulated  $J_{sc}$  vs. perovskite layer thickness of the normal-type device with a fixed ETL thickness of 100 nm. Device structure: ITO (140 nm)/PEDOT : PSS (40 nm)/perovskite (0–1000 nm)/PC<sub>60</sub>BM (100 nm)/Ag (120 nm). (c) The contour plot of simulated

pathways.<sup>51</sup> Although the nature of thin-film perovskite on PEDOT : PSS may be different from that on ZnO or TiO<sub>2</sub>, we believe that the optical constants are not too much sensitive to the nature of the interface. Thus, a negligible difference in perovskite optical constants on different underlayers is assumed in the optical simulation. Fig. 4(a) shows the contour plot of the simulated  $J_{sc}$  vs. perovskite and the PC<sub>60</sub>BM thicknesses of a normal-type device with a ITO(140 nm)/PEDOT : PSS(40 nm)/perovskite/PC<sub>60</sub>BM/Ag(120 nm) structure.

For better carrier extraction, some studies have reported the incorporation of several nanometre organic layers (*e.g.*, bathocuproine (BCP) or 4,7-diphenyl-1,10-phenanthroline (Bphen)) or LiF or metals (*e.g.*, Ca, Ba) between the PC<sub>60</sub>BM and Ag interface. However, because the thicknesses of these interfacial layers are relatively thin compared to the perovskite and fullerene layers, they are expected to have a negligible optical effect (see Fig. S8†). Fig. 4(b) shows the simulated  $J_{sc}$  vs. perovskite layer thickness with a fixed ETL thickness of 100 nm. After a rapid increase in  $J_{sc}$  with respect to the perovskite thickness in the thickness range of 0 to 115 nm, the  $J_{sc}$  reaches a local maximum value of 17.12 mA cm<sup>−2</sup> at a layer thickness of 145 nm (point A). Rather than an increase in the  $J_{sc}$  value, a further increase in the perovskite layer thickness does not enhance the device performance. The second and third local maximum values of 20.65 and 21.73 mA cm<sup>−2</sup> are observed at a layer thicknesses of 275 (point B) and 435 nm (point C), respectively.  $J_{sc}$  tends to saturate to ~22.5 mA cm<sup>−2</sup> if the perovskite layer thickness is further increased to >1000 nm. The results clearly indicate a preferable perovskite layer thickness selection, in which the optical effect and carrier transportation should be simultaneously considered. Fig. 4(c) shows the contour plot of the simulated  $J_{sc}$  vs. perovskite and Spiro-OMeTAD thicknesses of the inverted device with a ITO(140 nm)/ZnO(40 nm)/perovskite/Spiro-OMeTAD/Ag(120 nm) structure. Unlike PEDOT : PSS( $n \sim 1.5$ ) used in the normal structure, the ETLs used in the inverted cell generally possess a higher refractive index. This results in a higher local maximum  $J_{sc}$  (18.86, 21.37 and 22.19 mA cm<sup>−2</sup> at a perovskite layer thicknesses of 165 nm (point D), 305 nm (point E) and 460 nm (point F), respectively) and a higher saturation  $J_{sc}$  (22.9 mA cm<sup>−2</sup>) achieved in inverted solar cells compared to the normal-type counterpart, as shown in Fig. 4(b) and (d). This effect can be attributed to better matches of the refractive indices between the ITO( $n \sim 2$ )/ZnO( $n \sim 2$ ) and ZnO( $n \sim 2$ )/perovskite( $n \sim 2.5$ ) interfaces. Due to the similar refractive indices of ZnO and TiO<sub>2</sub>

$J_{sc}$  vs. perovskite and Spiro-OMeTAD thicknesses of the inverted-type device. Device structure: ITO (140 nm)/ZnO (40 nm)/perovskite (0–1000 nm)/Spiro-OMeTAD (0–500 nm)/Ag (120 nm). (d) The simulated  $J_{sc}$  vs. perovskite layer thickness of the inverted-type device with a fixed HTL thickness of 300 nm. Device structure: ITO (140 nm)/ZnO (40 nm)/perovskite (0–1000 nm)/Spiro-OMeTAD (300 nm)/Ag (120 nm). (e) The E.Q.E. and reflective spectrum of the normal- and inverted-type devices, respectively. The normal-type device structure: ITO (140 nm)/PEDOT : PSS (40 nm)/perovskite (435 nm)/PC<sub>60</sub>BM (100 nm)/Ag (120 nm). The inverted-type device structure: ITO (140 nm)/ZnO (40 nm)/perovskite (460 nm)/Spiro-OMeTAD (300 nm)/Ag (120 nm).



( $n \sim 2$ ) and the similar refractive indices of organic HTL (Spiro-OMeTAD, *N,N'*-bis(naphthalen-1-yl)-*N,N'*-bis(phenyl)-benzidine (NPB), 4',4''-tris(carbazol-9-yl)triphenylamine (TCTA), di-[4-(*N,N*-ditolyl-amino)-phenyl] cyclohexane (TAPC)...etc.,  $n \sim 1.7$ ), the simulation results reported here can readily be applied to devices with  $\text{TiO}_2$  as the ETL and other organic materials as HTLs. As shown in Fig. 4(e), the mismatch in the reflective indices of the normal-type device causes a higher reflection and thus lower E.Q.E. across the entire wavelength range compared to the inverted cell. The results do not necessarily indicate that the normal-type structure is inferior to the inverted structure. One can achieve similar high  $J_{sc}$  and low reflection if low refractive index PEDOT : PSS can be replaced by higher refractive index HTLs (*cf.*  $\text{MoO}_3$ ,  $\text{WO}_3$ ...etc.) (see Fig. S9†). Recently, a  $\sim 80\%$  fill factor (FF) and open circuit voltage ( $V_{oc}$ ) as high as  $\sim 1.1$  V were obtained in  $\text{CH}_3\text{NH}_3\text{PbI}_3$  and  $\text{CH}_3\text{NH}_3\text{PbI}_{3-x}\text{Cl}_x$  solar cells. With the calculated achievable  $J_{sc}$  of  $22.6 \text{ mA cm}^{-2}$  at the practical thickness of 615 nm in the inverted-type device, PCEs of 20% can be anticipated with the proper designs depicted in this work.

Organometal halide perovskites have been found to simultaneously possess high absorption and a long carrier diffusion length of hundreds of nanometres. It is interesting to study the result of the tandem cell configuration if the parameters such as layer thicknesses can be freely altered. As shown in Fig. 3, the tandem cell with the structure glass/ITO(140 nm)/ZnO(20 nm)/front perovskite layer ( $T_{\text{front}}$  nm)/Spiro-OMeTAD(100 nm)/Ag(1 nm)/ZnO(20 nm)/back perovskite layer ( $T_{\text{back}}$  nm)/Spiro-OMeTAD(100 nm)/Ag was employed in the calculation. For each perovskite layer pair, the thicknesses of both the front ( $T_{\text{front}}$  between 0 and 300 nm) and the back ( $T_{\text{back}}$  between 0 and 800 nm) layers were varied, and the integrated  $J_{sc}$  in these layers under 1 sun AM 1.5G was calculated. The contour plot of mismatched  $J_{sc}$  values is shown in Fig. 5(a). A positive  $J_{sc}$  mismatch indicates that the  $J_{sc}$  of the front cell is higher than that of the back cell, whereas a negative  $J_{sc}$  mismatch value means that the  $J_{sc}$  of the back cell is higher than that of the front cell. The isoline, shown in the Fig. 5(a), displays the optimised thicknesses of the front and back perovskite layers, where  $J_{sc,\text{front}} = J_{sc,\text{back}}$  assuming that each cell exhibits 100% internal quantum efficiency and the same FF. A better visualisation of the quantitative effect of the front and back layer thicknesses is presented in Fig. 5(b). This figure shows the  $J_{sc,\text{front}}$  and  $J_{sc,\text{back}}$  vs.  $T_{\text{back}}$  with a fixed  $T_{\text{front}}$  of 45 nm, 90 nm, and 135 nm. It is clear that if a thicker front perovskite layer (135 nm) is used; the front layer absorbs most of the photons and  $J_{sc,\text{back}}$  can never catch up with  $J_{sc,\text{front}}$  even with a very thick back layer thickness of  $>800$  nm. In contrast, because a thinner front perovskite layer (45 nm) is utilised, there is only one interception of the  $J_{sc,\text{front}}$  and  $J_{sc,\text{back}}$  lines with  $J_{sc,\text{front}} = J_{sc,\text{back}} = 8.0 \text{ mA cm}^{-2}$  at  $T_{\text{back}} = 88$  nm. The best  $J_{sc}$  achieved in both the  $T_{\text{front}} = 135$  nm and 45 nm designs is far less than half of the optimised single cell. Interestingly, however, with  $T_{\text{front}} = 90$  nm,  $J_{sc,\text{front}}$  matches  $J_{sc,\text{back}}$  with a value of  $\sim 11.5 \text{ mA cm}^{-2}$  across a wide range of  $T_{\text{back}}$  from 350 nm to  $>800$  nm. This remarkable result indicates a wide process window for perovskite-based tandem cells. If the thickness of the front perovskite layer can be more precisely

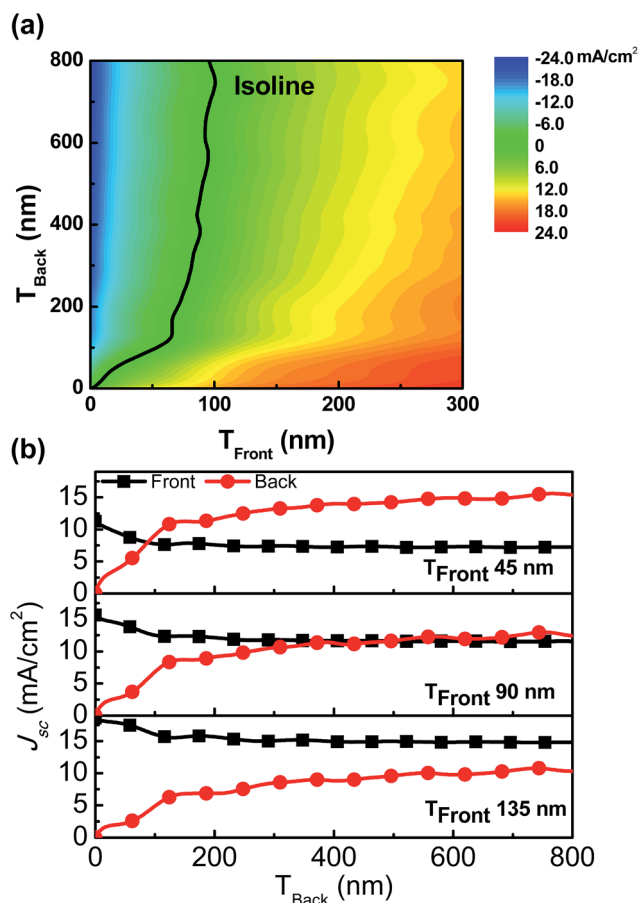


Fig. 5 (a) The contour plot of mismatched  $J_{sc}$  values. The black isoline indicates the condition in which  $J_{sc,\text{front}} = J_{sc,\text{back}}$ . Device structure: ITO (140 nm)/ZnO (20 nm)/front perovskite layer (0–300 nm)/Spiro-OMeTAD (100 nm)/Ag (1 nm)/ZnO (20 nm)/back perovskite layer (0–800 nm)/Spiro-OMeTAD (100 nm)/Ag (120 nm). (b)  $J_{sc,\text{front}}$  and  $J_{sc,\text{back}}$  vs.  $T_{\text{back}}$  with a fixed  $T_{\text{front}}$  of 45 nm, 90 nm, and 135 nm.

controlled, a wide range of the back perovskite layer thickness is tolerable for obtaining optimised performance. With  $\sim 80\%$  FF and  $V_{oc} \sim 2.2$  V (two times that of the single cell), PCEs of 20% can also be obtained. The maximum efficiency achievable in the tandem cell is approximate to the single cell, which is understandable because the high extinction coefficient perovskite thin layer can potentially absorb most of the photons by a single layer. The advantage of such a tandem cell utilising the same perovskite active layer in front and back cells is a higher  $V_{oc}$  of  $>2$  V, which could readily be used in water splitting.<sup>52,53</sup> A more practical approach to achieving a higher PCE in tandem cells should be to utilise the spectrum complementary front and back cell material, either small and large bandgap perovskites or perovskite with other organic (*cf.* APFO-Green1, PbPc) or inorganic (*cf.* Si, CIGS, CZTS) materials.<sup>54–56</sup>

To demonstrate the applicability of the perovskite optical constants obtained in this study and of the panchromatic optical simulation program, the perovskite/CIGS tandem cells were optimised. The wavelength-dependent optical constants of CIGS were adopted from the literature,<sup>39</sup> and the common

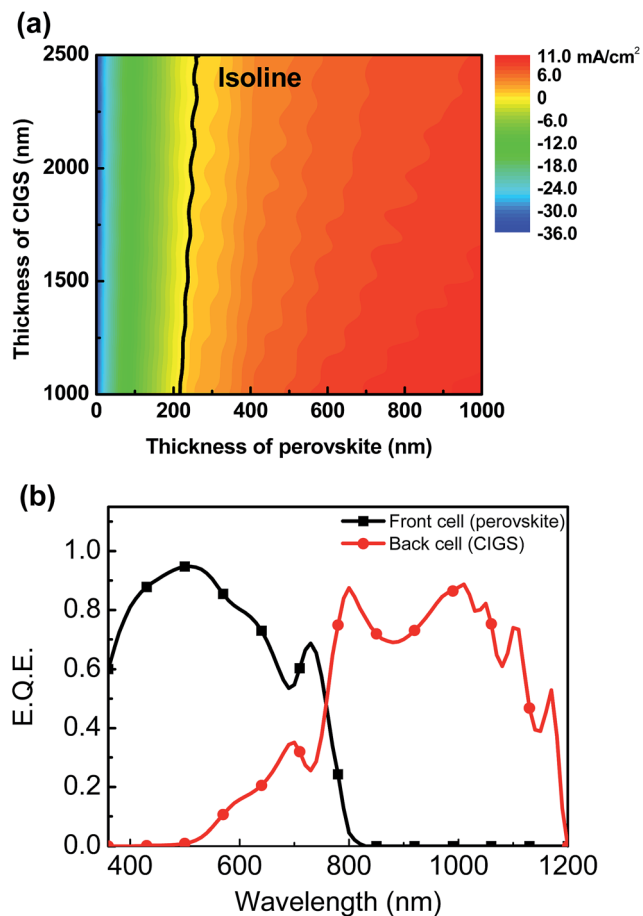


Fig. 6 (a) The contour plot of mismatched  $J_{sc}$  values. The black isoline indicates the condition in which  $J_{sc, \text{front}} = J_{sc, \text{back}}$ . Device structure: AZO (50 nm)/ $\text{C}_{60}$  (10 nm)/front perovskite layer (0–1000 nm)/ $\text{MoO}_3$  (5 nm)/AZO (200 nm)/ZnO (60 nm)/ZnS (20 nm)/back CIGS layer (1000–2500 nm)/Mo (1000 nm) (b) E.Q.E. spectra of front cell (perovskite) and back cell (CIGS) in optimised perovskite–CIGS tandem devices. Device structure: AZO (50 nm)/ $\text{C}_{60}$  (10 nm)/front perovskite layer (270 nm)/ $\text{MoO}_3$  (5 nm)/AZO (220 nm)/ZnO (60 nm)/ZnS (20 nm)/back CIGS layer (2500 nm)/Mo (1000 nm).

Mo/CIGS/ZnS/ZnO/AZO structure of the CIGS solar cell was used. The perovskite/CIGS tandem cell structure is shown in Fig. 3. Fig. 6(a) shows the thickness relationship for reaching equal  $J_{sc}$  values in the front and the back cell. The matched  $J_{sc}$  occurred when the thickness of the perovskite film was in the range of 200 to 300 nm. The thicknesses of the perovskite layer, CIGS layer and interconnection AZO layer were further varied freely to acquire the highest  $J_{sc}$  (see Fig. S10†). Fig. 6(b) shows the optimised E.Q.E. spectra of the front perovskite and the CIGS cells. With a perovskite layer thickness of 270 nm, a CIGS layer thickness of 2500 nm and an AZO layer thickness of 220 nm, complementary absorptions occurred across the entire 300 to 1200 nm wavelength range and balanced  $J_{sc, \text{front}} = J_{sc, \text{back}} = 19.1 \text{ mA cm}^{-2}$ . With an estimated  $V_{oc}$  of 1.8 V (1.1 V from the perovskite cell and 0.7 V from the CIGS cell) and an F.F. of 80%, a very promising PCE up to 29% can be anticipated. The efficiency is 45% higher than the recorded perovskite and CIGS cell efficiencies.<sup>57,58</sup> Note that due to the raw material and

fabrication costs of perovskite solar cells, perovskite/CIGS tandem cells could be a very attractive next-generation power source with a reasonable production cost and large-area manufacturing capacity.

The band gap engineering for perovskite has been demonstrated by substituting the elements.<sup>3,16,56</sup> Owing to the lack of optical constants of other perovskites, it is difficult to accurately estimate the maximum potential of perovskite/perovskite tandem cells with two perovskites of different band gaps. However, since the wavelength coverage of perovskite/CIGS tandem cells is much larger than that of perovskite/perovskite tandem cells, a 22–25% PCE could probably be anticipated in the perovskite/perovskite tandem devices which is lower than that of the perovskite/CIGS ones.

## Conclusions

In conclusion, the optical constants of a  $\text{CH}_3\text{NH}_3\text{PbI}_{3-x}\text{Cl}_x$  perovskite thin film were acquired for the first time over the wavelength range of 300 to 1100 nm using VASE. An oscillator model that consisted of five Gaussian absorptions and EMA layers was used to accurately model the perovskite thin film. The  $\text{CH}_3\text{NH}_3\text{PbI}_{3-x}\text{Cl}_x$  thin film exhibits a remarkably high extinction coefficient and a relatively low refractive index across the UV to near-infrared region. The detailed optical constant information obtained in this work can be used in the structure design of perovskite photovoltaics. The optimum performance of single and tandem planar-type perovskite solar cells was simulated. The simulation results indicated that a high refractive index ETL or HTL should be used between the transparent electrode and the perovskite active layer to lower the reflection caused by the ITO/ETL(HTL) and ETL(HTL)/perovskite interface. Our calculations suggest that PCEs of up to 20% and 29% are feasible without any antireflection and light scattering structures in single and perovskite/CIGS tandem cells given a proper device structure design. The calculation also indicated that even in optically optimised cells, an average reflection of  $\sim 10\%$  existed in both single and perovskite/CIGS tandem cells (see Fig. S9 and S11†); a proper integration of an antireflection optical structure to lower the reflection of the devices can most likely further increase the device performance. We believe that the optical designs presented here provide a guideline to further enhance the efficiency of perovskite solar cells beyond 20–30%. The practical and precise estimation also revealed the potential and limitations of perovskite-based photovoltaics. More importantly, the optical constants of perovskites presented in this paper also provide the most relevant parameters for device designers and engineers to design and fabricate not only planar but also nanostructured perovskite solar cells with extremely high efficiencies.

## Acknowledgements

The authors would like to acknowledge the assistance of James Hilfiker of the J. A. Woollam Co. in ellipsometric data analysis and the financial support from the Ministry of Science and Technology of Taiwan (102-2221-E-007-125-MY3,

101-2112-M-007-017-MY3, 102-2633-M-007-002, and 103-3113-E-007-004) and the Low Carbon Energy Research Center, National Tsing Hua University.

## Notes and references

- 1 A. Kojima, K. Teshima, Y. Shirai and T. Miyasaka, *J. Am. Chem. Soc.*, 2009, **131**, 6050–6051.
- 2 P. Qin, S. Tanaka, S. Ito, N. Tetreault, K. Manabe, H. Nishino, M. K. Nazeeruddin and M. Grätzel, *Nat. Commun.*, 2014, **5**, 3834.
- 3 J. H. Noh, S. H. Im, J. H. Heo, T. N. Mandal and S. I. Seok, *Nano Lett.*, 2013, **13**, 1764–1769.
- 4 J. M. Ball, M. M. Lee, A. Hey and H. J. Snaith, *Energy Environ. Sci.*, 2013, **6**, 1739–1743.
- 5 J. Burschka, N. Pellet, S. J. Moon, R. Humphry-Baker, P. Gao, M. K. Nazeeruddin and M. Grätzel, *Nature*, 2013, **499**, 316–319.
- 6 S. Ryu, J. H. Noh, N. J. Jeon, Y. Chan Kim, W. S. Yang, J. Seo and S. I. Seok, *Energy Environ. Sci.*, 2014, **7**, 2614–2618.
- 7 N. Pellet, P. Gao, G. Gregori, T.-Y. Yang, M. K. Nazeeruddin, J. Maier and M. Grätzel, *Angew. Chem., Int. Ed.*, 2014, **53**, 3151–3157.
- 8 M. M. Lee, J. Teuscher, T. Miyasaka, T. N. Murakami and H. J. Snaith, *Science*, 2012, **338**, 643–647.
- 9 J.-Y. Jeng, K.-C. Chen, T.-Y. Chiang, P.-Y. Lin, T.-D. Tsai, Y.-C. Chang, T.-F. Guo, P. Chen, T.-C. Wen and Y.-J. Hsu, *Adv. Mater.*, 2014, **26**, 4107–4113.
- 10 Y. H. Hu, *Adv. Mater.*, 2014, **26**, 2102–2104.
- 11 A. Yella, L. P. Heiniger, P. Gao, M. K. Nazeeruddin and M. Grätzel, *Nano Lett.*, 2014, **14**, 2591–2596.
- 12 C. Roldan-Carmona, O. Malinkiewicz, A. Soriano, G. Minguez Espallargas, A. Garcia, P. Reinecke, T. Kroyer, M. I. Dar, M. K. Nazeeruddin and H. J. Bolink, *Energy Environ. Sci.*, 2014, **7**, 994–997.
- 13 M. Liu, M. B. Johnston and H. J. Snaith, *Nature*, 2013, **501**, 395–398.
- 14 Q. Chen, H. Zhou, Z. Hong, S. Luo, H. S. Duan, H. H. Wang, Y. Liu, G. Li and Y. Yang, *J. Am. Chem. Soc.*, 2014, **136**, 622–625.
- 15 P. Docampo, J. M. Ball, M. Darwich, G. E. Eperon and H. J. Snaith, *Nat. Commun.*, 2013, **4**, 2761.
- 16 G. E. Eperon, S. D. Stranks, C. Menelaou, M. B. Johnston, L. M. Herz and H. J. Snaith, *Energy Environ. Sci.*, 2014, **7**, 982–988.
- 17 P.-W. Liang, C.-Y. Liao, C.-C. Chueh, F. Zuo, S. T. Williams, X.-K. Xin, J. Lin and A. K. Y. Jen, *Adv. Mater.*, 2014, **26**, 3748–3754.
- 18 D. Liu and T. L. Kelly, *Nat. Photonics*, 2014, **8**, 133–138.
- 19 J. You, Z. Hong, Y. Yang, Q. Chen, M. Cai, T.-B. Song, C.-C. Chen, S. Lu, Y. Liu, H. Zhou and Y. Yang, *ACS Nano*, 2014, **8**, 1674–1680.
- 20 K.-G. Lim, H.-B. Kim, J. Jeong, H. Kim, J. Y. Kim and T.-W. Lee, *Adv. Mater.*, 2014, **26**, 6461–6466.
- 21 F. Zuo, S. T. Williams, P.-W. Liang, C.-C. Chueh, C.-Y. Liao and A. K. Y. Jen, *Adv. Mater.*, 2014, **26**, 6454–6460.
- 22 C.-W. Chen, H.-W. Kang, S.-Y. Hsiao, P.-F. Yang, K.-M. Chiang and H.-W. Lin, *Adv. Mater.*, 2014, **26**, 6647–6652.
- 23 D. F. S. Petri, *J. Braz. Chem. Soc.*, 2002, **13**, 695–699.
- 24 M. D. Rovenia Pascu, *Rom. Rep. Phys.*, 2012, **64**, 135–142.
- 25 T. E. Tiwald, D. W. Thompson, J. A. Woollam, W. Paulson and R. Hance, *Thin Solid Films*, 1998, **313–314**, 661–666.
- 26 Y. S. Jung, *Thin Solid Films*, 2004, **467**, 36–42.
- 27 R. A. Synowicki, *Thin Solid Films*, 1998, **313–314**, 394–397.
- 28 L. A. A. Pettersson, T. Johansson, F. Carlsson, H. Arwin and O. Inganäs, *Synth. Met.*, 1999, **101**, 198–199.
- 29 J. G. E. Jellison, *Thin Solid Films*, 1998, **313–314**, 33–39.
- 30 R. M. A. Azzam and N. M. Bashara, *Ellipsometry and Polarized Light*, North Holland, Amsterdam, NL, 1977.
- 31 H.-W. Lin, C.-L. Lin, C.-C. Wu, T.-C. Chao and K.-T. Wong, *Org. Electron.*, 2007, **8**, 189–197.
- 32 H.-W. Lin, C.-L. Lin, H.-H. Chang, Y.-T. Lin, C.-C. Wu, Y.-M. Chen, R.-T. Chen, Y.-Y. Chien and K.-T. Wong, *J. Appl. Phys.*, 2004, **95**, 881–886.
- 33 K. Järrendahl and H. Arwin, *Thin Solid Films*, 1998, **313–314**, 114–118.
- 34 C. M. Herzinger, B. Johs, W. A. McGahan, J. A. Woollam and W. Paulson, *J. Appl. Phys.*, 1998, **83**, 3323–3336.
- 35 C. M. Herzinger, H. Yao, P. G. Snyder, F. G. Celii, Y. C. Kao, B. Johs and J. A. Woollam, *J. Appl. Phys.*, 1995, **77**, 4677–4687.
- 36 D. E. Aspnes, J. B. Theeten and F. Hottier, *Phys. Rev. B: Condens. Matter Mater. Phys.*, 1979, **20**, 3292–3302.
- 37 H. Fujiwara, J. Koh, P. I. Rovira and R. W. Collins, *Phys. Rev. B: Condens. Matter Mater. Phys.*, 2000, **61**, 10832–10844.
- 38 G. E. Jellison, M. F. Chisholm and S. M. Gorbalkin, *Appl. Phys. Lett.*, 1993, **62**, 3348–3350.
- 39 P. D. Paulson, R. W. Birkmire and W. N. Shafarman, *J. Appl. Phys.*, 2003, **94**, 879–888.
- 40 S. Adachi, *J. Appl. Phys.*, 1989, **66**, 6030–6040.
- 41 S. Adachi, T. Kimura and N. Suzuki, *J. Appl. Phys.*, 1993, **74**, 3435–3441.
- 42 Y.-H. Chen, C.-W. Chen, Z.-Y. Huang, K.-T. Wong, L.-Y. Lin, F. Lin and H.-W. Lin, *Org. Electron.*, 2014, **15**, 1828–1835.
- 43 Y.-H. Chen, C.-W. Chen, Z.-Y. Huang, W.-C. Lin, L.-Y. Lin, F. Lin, K.-T. Wong and H.-W. Lin, *Adv. Mater.*, 2014, **26**, 1129–1134.
- 44 J.-H. Chang, H.-F. Wang, W.-C. Lin, K.-M. Chiang, K.-C. Chen, W.-C. Huang, Z.-Y. Huang, H.-F. Meng, R.-M. Ho and H.-W. Lin, *J. Mater. Chem. A*, 2014, **2**, 13398–13406.
- 45 L. A. A. Pettersson, L. S. Roman and O. Inganäs, *J. Appl. Phys.*, 1999, **86**, 487–496.
- 46 C. Yasuo, I. Ashraful, W. Yuki, K. Ryoichi, K. Naoki and H. Liyuan, *Jpn. J. Appl. Phys.*, 2006, **45**, L638.
- 47 C.-W. Chen, Z.-Y. Huang, Y.-M. Lin, W.-C. Huang, Y.-H. Chen, J. Strzalka, A. Y. Chang, R. D. Schaller, C.-K. Lee, C.-W. Pao and H.-W. Lin, *Phys. Chem. Chem. Phys.*, 2014, **16**, 8852–8864.
- 48 V. Shrotriya, G. Li, Y. Yao, C.-W. Chu and Y. Yang, *Appl. Phys. Lett.*, 2006, **88**, 073508.
- 49 S. Han, W. S. Shin, M. Seo, D. Gupta, S.-J. Moon and S. Yoo, *Org. Electron.*, 2009, **10**, 791–797.

- 50 J.-Y. Jeng, Y.-F. Chiang, M.-H. Lee, S.-R. Peng, T.-F. Guo, P. Chen and T.-C. Wen, *Adv. Mater.*, 2013, **25**, 3727–3732.
- 51 S. Colella, E. Mosconi, G. Pellegrino, A. Alberti, V. L. P. Guerra, S. Masi, A. Listorti, A. Rizzo, G. G. Condorelli, F. De Angelis and G. Gigli, *J. Phys. Chem. Lett.*, 2014, **5**, 3532–3538.
- 52 M. G. Walter, E. L. Warren, J. R. McKone, S. W. Boettcher, Q. Mi, E. A. Santori and N. S. Lewis, *Chem. Rev.*, 2010, **110**, 6446–6473.
- 53 J. R. Bolton, *Sol. Energy*, 1996, **57**, 37–50.
- 54 X. Wang, E. Perzon, J. L. Delgado, P. de la Cruz, F. Zhang, F. Langa, M. Andersson and O. Inganäs, *Appl. Phys. Lett.*, 2004, **85**, 5081–5083.
- 55 M. Hiramoto, K. Kitada, K. Iketaki and T. Kaji, *Appl. Phys. Lett.*, 2011, **98**, 023302.
- 56 M. H. Kumar, S. Dharani, W. L. Leong, P. P. Boix, R. R. Prabhakar, T. Baikie, C. Shi, H. Ding, R. Ramesh, M. Asta, M. Graetzel, S. G. Mhaisalkar and N. Mathews, *Adv. Mater.*, 2014, **26**, 7122–7127.
- 57 H. Zhou, Q. Chen, G. Li, S. Luo, T.-b. Song, H.-S. Duan, Z. Hong, J. You, Y. Liu and Y. Yang, *Science*, 2014, **345**, 542–546.
- 58 P. Jackson, D. Hariskos, R. Wuerz, W. Wischmann and M. Powalla, *Phys. Status Solidi RRL*, 2014, **8**, 219–222.